Supplementary material for

Droplet impact dynamics on shallow pools

Thomas C. Sykes[1]†, Radu Cimpeanu[2], Ben D. Fudge[1], J. Rafael Castrejón-Pita[3]‡, and Alfonso A. Castrejón-Pita[1]¶

[1]Department of Engineering Science, University of Oxford, Oxford OX1 3PJ, UK

[2]Mathematics Institute, University of Warwick, Coventry CV4 7AL, UK

[3]Department of Mechanical Engineering, University College London, London WC1E 7JE, UK

CONTENTS

§1. Pool construction

The experimental setup is described in section 2.1 of the main text, and depicted in figures 1b and S1. Here we provide further technical data and explanation.

We constructed the pool from transparent material so that the light source for the high-speed camera could be positioned behind the higher back panel. Specifically, we used clear polystyrene due to its chemical resistance to ethanol. However, the contact angle of ethanol on clear polystyrene is relatively low, so a meniscus forms on the side wall of the pool that was found to be problematic to image through in earlier design iterations. Others have overcome this problem by slightly overfilling the pool in order to pin the contact line on the rim (e.g. Bisighini *et al.*, Phys. Rev. E, **82** 036319, 2010), but we found this to be impractical whilst controllably varying the pool depth (especially for small h^*). The 'infinity pool' construction, which enables an unobstructed view of the impact site for the side-view high speed camera (see the setup as viewed from this perspective in figure S1), was therefore essential to achieve good image quality in the region the ejecta sheet resides, *just* above the free surface.

The rectangular main compartment of the pool measured $103 \times 32 \times 20$ mm^3, with higher back and side panels ensuring flow out only into the front trough. The Z bracket that held the untreated glass slide (76×26 mm^2 horizontally), which served as the effective pool base, was 3D printed. CAD files for both the pool (as an example – we cut the actual panels with a band saw) and Z bracket can be found in our dedicated GitHub repository for this work. The pool and effective base sizes were driven by two factors. First, a desire to ensure that the impact site was far enough from the pool walls (and co-located free surface menisci) so they had no significant effect on the dynamics of interest. Second, the cylindrical sensor for the confocal chromatic measuring system (see the next section) was 54 mm in diameter – the falling droplet had to pass the sensor, which necessitated an increased pool width relative to the first consideration. We chose to limit the maximum pool depth studied to $h^* \approx 2$ due to

† Email address for correspondence: thomas.sykes@eng.ox.ac.uk; t.c.sykes@outlook.com
‡ Email address for correspondence: r.pita@ucl.ac.uk; castrejon@cantab.net
¶ Email address for correspondence: alfonso.castrejon-pita@wadham.ox.ac.uk

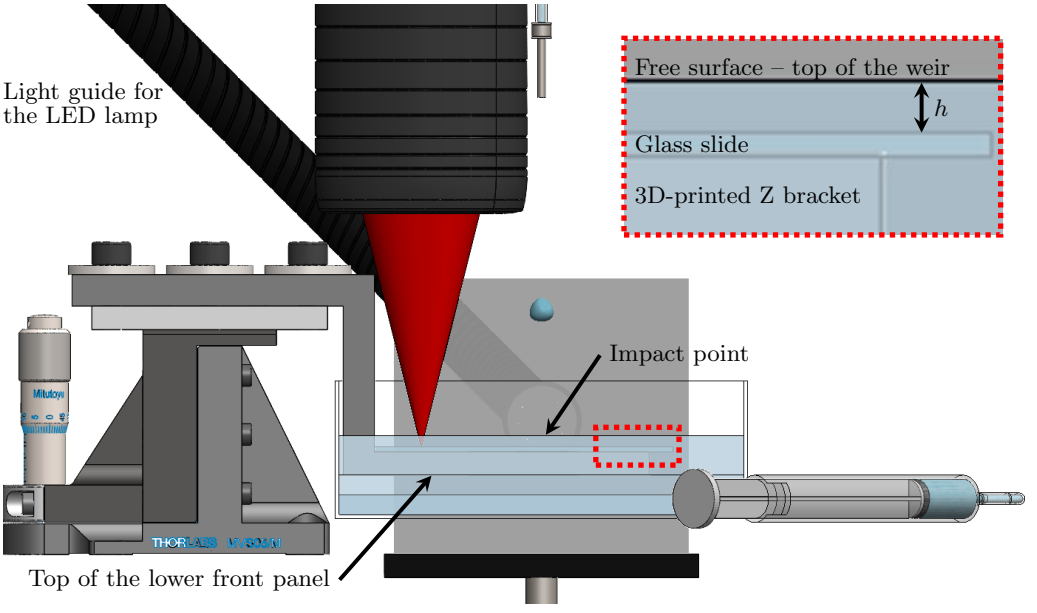

Figure S1: View of the experimental setup from the high-speed camera. Note the unobstructed view of the impact site – the top of the lower front panel is far below the free surface. The red cone (invisible to the naked eye) depicts the light beam associated with the confocal chromatic measuring system, which is used to determine the pool depth h. This beam is focused onto the glass surface by a multi-lens optical system within the cylindrical sensor housing.

prior knowledge (see main text) that at this depth the pool base would not play a significant role in the early-time dynamics of interest (i.e. be considered a deep pool here). Secondary factors included the range of the specific confocal sensor employed to measure h and a desire to reduce the total fluid volume required.

§2. Pool depth measurement using a confocal system

For every experiment, the pool depth on impact h was determined using a Micro-Epsilon confocal chromatic measuring system consisting of an IFC2421 controller and IFS2405-10 sensor. The sensor is shown in figure S1, along with a depiction of its light beam, which was focused on the effective pool base. The sensor was used to measure a one-sided thickness between the free surface and pool base, which was possible up to ~ 6 mm for ethanol. As seen in figure S2, we read out the relative displacement (accounting for the different refractive indices of ethanol and air) of the free surface and pool base from the sensor separately at 2 Hz until impact. We designed a MATLAB code to automatically determine h from these saved data, which is provided in our GitHub repository. Figure S2 shows the results of a typical analysis, for which $h = 0.19$ mm.

To determine the relative displacement of the pool base from the sensor at $t = 0$, we first analysed the raw pool base data (black markers in figure S2) to identify abrupt changes in variance (vertical dashed green lines in figure S2), corresponding to deliberate Z bracket adjustments or abnormalities. We chose a low threshold (i.e. high sensitivity) to reduce false negatives. After the final abrupt change, the pool base was considered fixed and we took the median of these data to be the relative displacement at $t = 0$ (solid green line in figure S2).

We manually overfilled the pool prior to each experiment so that the free surface was clearly visible on impact. Hence the relative displacement of the free surface from the sensor

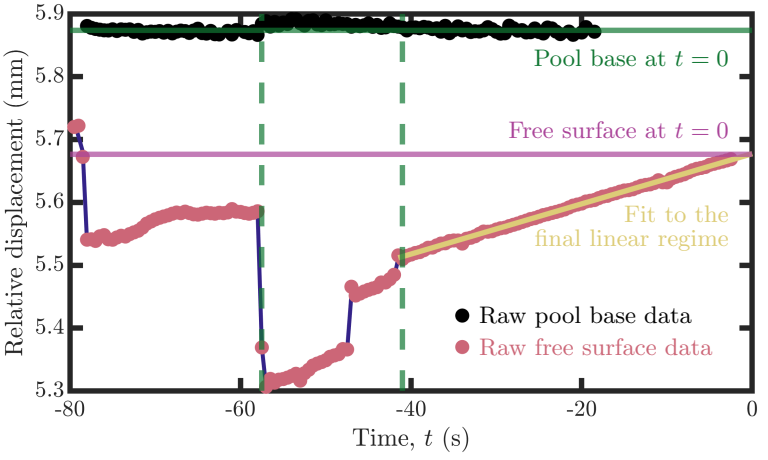

Figure S2: Raw and processed confocal data of a typical experiment, for which $h = 0.19$ mm. Dashed vertical green lines identify significant changes in the variance of the pool base data (high sensitivity); yellow and indigo lines are fits in linear regimes of the free surface data. $t = 0$ on impact.

typically had a slowly increasing linear trend (red markers in figure S2) when the pool was not being actively filled or drained. We therefore sought to identify abrupt changes in linear regimes (instead of variance) for the raw free surface data. Linear fits corresponding to each regime identified are the solid indigo lines in figure S2. The final linear fit (solid yellow line in figure S2) was used to identify the relative displacement of the free surface from the sensor at $t = 0$ (solid purple line) by evaluating it at the time of impact encoded in the high-speed camera data.

The difference between the relative displacements at $t = 0$ (solid green and purple lines in figure S2) is h. A key advantage of analysing the pool base and free surface separately was the ability to determine h even at depths where the confocal system could not distinguish between them ($h \lessapprox 0.35$ mm, depending on the exact sensor placement). At such depths, the confocal system reverted to a relative displacement measurement of the interface closer to the sensor only. In this case, the closer interface was the continuously varying free surface – see figure S2, where the static pool base data ends at $t \approx -20$ s.

We verified the indicated pool thickness by making known adjustments to the effective pool base height via the vertical translation stage, when the free surface well below the top of the weir (to maintain a consistent free surface level), and compared these to the value of h as determined using the method described above. We also checked instantaneous thickness measurements before and after each set of experiments undertaken to ensure the correct experiment setup (especially that appropriate material properties had being set in the confocal system's controller). The confocal system was controlled (started, stopped, etc) by TTL signals linking it with the high-speed camera, LED light shutter, and syringe pumps.

§3. Additional impact images

Figure S3 supplements figure 3 in the main text, containing raw experimental images for 7 additional depths $h^* \in [0.08, 0.28]$ spanning the depth transition. The Weber number is essentially fixed, but with a slightly wider range $We = 345 \pm 10$ compared to figure 3, except panel g where $We = 330$. Each column within figure S3 corresponds to the same t_u^* (listed in the caption), which are accurate to ± 0.01 due to small variations in D/u depending on the precise velocity & radius of curvature of each droplet. All experiments within a given

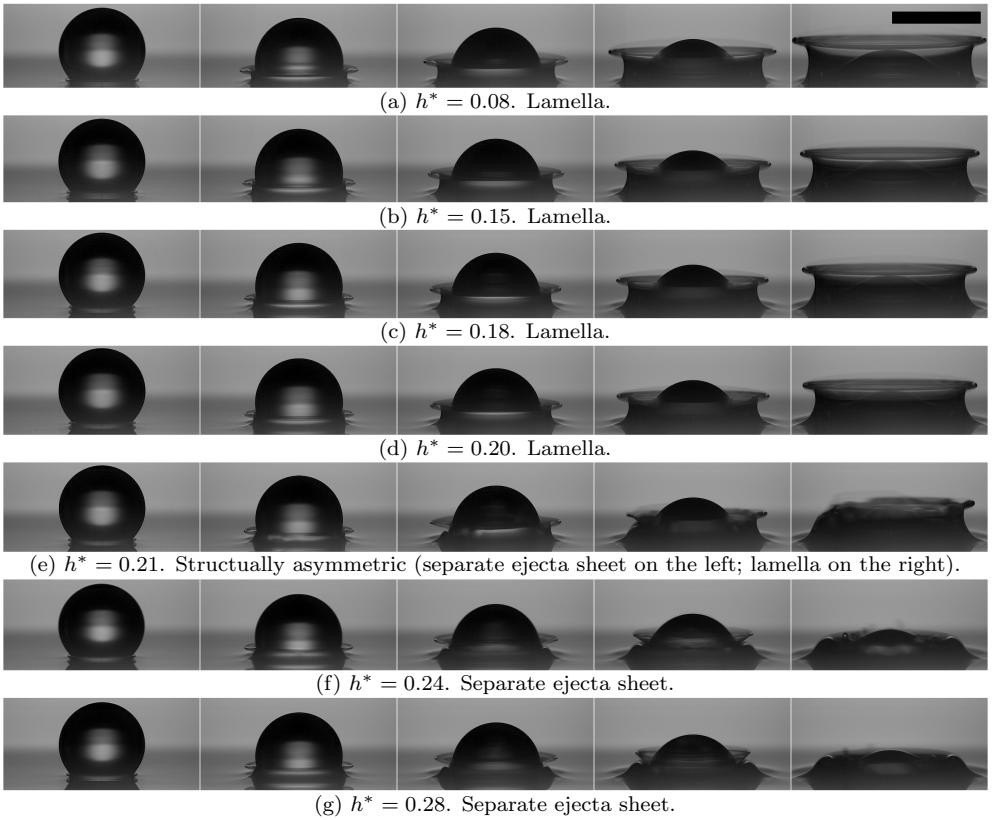

(a) $h^* = 0.08$. Lamella.

(b) $h^* = 0.15$. Lamella.

(c) $h^* = 0.18$. Lamella.

(d) $h^* = 0.20$. Lamella.

(e) $h^* = 0.21$. Structually asymmetric (separate ejecta sheet on the left; lamella on the right).

(f) $h^* = 0.24$. Separate ejecta sheet.

(g) $h^* = 0.28$. Separate ejecta sheet.

Figure S3: Impact of an ethanol droplet onto a shallow pool of the same fluid. Here $We = 345 \pm 10$, except panel g for which $We = 330$. The bottom of each image coincides with the pool base, whilst the distance shown above the pool is fixed (1.83 mm). The times t_u^* corresponding to each frame are 0.09, 0.20, 0.31, 0.45, and 0.65, respectively (accurate to ±0.01). All panels share a common 2 mm scale bar.

outcome (lamella or separate ejecta sheet) are qualitatively similar, whilst signatures of both regimes (i.e. structurally asymmetric dynamics) are seen at $h^* = 0.21$ close to the depth transition. Figure S3 therefore provides visual experimental evidence for the abruptness of the depth transition and robustness of each impact outcome, as also evidenced by processed data in our regime map contained within the main text (figure 4).

§4. Additional supporting graphs

Additional graphs supporting the arguments made in sections 3.3 and 3.4 of the main text are found in figure S4. In particular, figure S4a provides a graphical representation of the liquid bridge building process that occurs on deeper pools ($h^* \geqslant 0.22$), via the difference in horizontal position of points C and D, $x_C - x_D$ (see figure 2c of the main text for definitions of the characteristic points). $x = 0$ on the axis of symmetry, and x_C and x_D are non-negative. Only for $h^* \geqslant 0.22$, the top of the ejecta base (point D) overtakes the bottom (point C) as a result of the bridge-building process between the ejecta sheet and droplet, and therefore $x_C - x_D$ turns negative. Hence these depths have the separate ejecta sheet impact outcome. This process can also be seen visually in figure 8c of the main text, where for both depths point D is almost coincident at $t_u^* = 0.033$, whilst by $t_u^* = 0.041$ it propagates further ahead

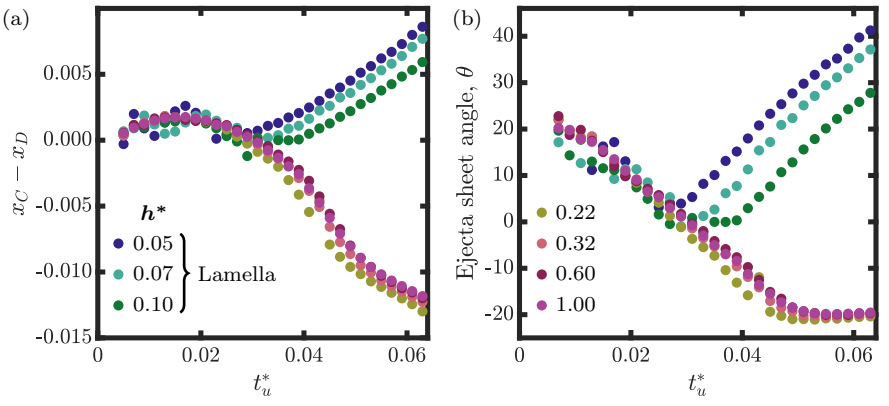

Figure S4: (a) The horizontal distance between points C and D, $x_C - x_D$, where $x = 0$ on the axis of symmetry ($x \geqslant 0$). This quantity provides a graphical representation of the liquid bridge building process for $h^* \geqslant 0.22$ with point D overtaking point C. (b) Ejecta sheet angle computed as the angle between the normal to the ejecta sheet base segment CD and the horizontal. *We* = 345 impact; $h^* \in [0.05, 1.00]$.

for the deeper case. Conversely, when a lamella is formed there is no bridge-building process and point C eventually propagates ahead of point D (so $x_C - x_D$ turns positive), leading to an increase in the ejecta sheet angle θ at a time matching the bifurcation in ejecta base thickness (see figure 8a of the main text).

Figure S4b shows the evolution of the ejecta sheet angle θ for all depths considered in this work, which is computed as the angle between the normal to the ejecta sheet base segment CD (and therefore directly related to figure S4a) and the horizontal. A similar graph was used by Thoraval *et al.* (Phys. Rev. Lett., **108** 264506, 2012) to show that the ejecta sheet angle is important in determining its subsequent dynamics for different *Re*. Note however that in that work the characteristic points were defined based on free surface curvature, instead of the parameterisation $\{x(s), y(s)\}$ as is done here (see section 2.3 of the main text). For all depths considered, figure S4b shows that the ejecta sheet angles are similar until the moment of ejecta sheet stretching for $h^* \leqslant 0.10$, corresponding to the bifurcation in figure 8a. This observation suggests that the ejecta sheet angle does not play a major role in the depth transition identified in this work.

§5. Velocity snapshots

The velocity snapshots mentioned in section 3.3 of the main text are found in figure S5. The simulations underpinning this figure are the same as those used to generate figure 6. For both pool depths, the overall velocity fields are similar at all times. The peak velocity is found in the air (the lower viscosity fluid), directed away from the impact site and slightly upwards. Since the velocity within the droplet is generally directed downward due to the initial condition, greater curvature in streamlines is required for flow from the droplet, compared to the flow from the pool, to be directed into the ejecta sheet.

§6. Video captions

Below we provide detailed captions for each of the supplementary videos (experimental and numerical):

- *Movies 1, 2, and 3*: Animations of the image montages found in figure 3 (main text): *We* = 345 at dimensionless pool depth $h^* = 0.10$ (movie 1); $h^* = 0.24$ (movie 2); $h^* = 0.32$

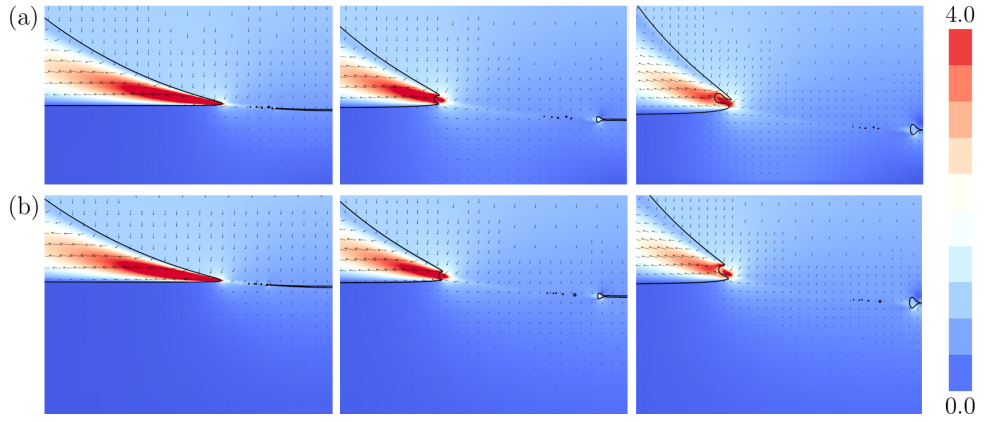

Figure S5: Evolution of the flow field and evolving interfaces following $We = 345$ impact, visualised in a subset of the computational domain with the normalised velocity field magnitude $|\mathbf{u}| = (u_r^2 + u_z^2)^{1/2}$ (background colour) and arrows indicating each velocity component. (a) $h^* = 0.10$; (b) $h^* = 0.32$. Frames are taken at $t_u^* = 0.003$ (left), $t_u^* = 0.023$ (centre) and $t_u^* = 0.043$ (right).

(movie 3). These images were captured at 37 000 fps with a pixel resolution of 1280×544, using a Phantom v2512. They have been cropped to 768×350, which covers approximately (6.2×2.8) mm in each animation. The videos play at 8 fps and contain 56 frames each, therefore show approximately 1.5 ms of real time, from $t = -0.2$ ms to $t = 1.4$ ms.

- *Movies 4 and 5*: Direct numerical simulation summaries of drop impact scenarios described by $We = 345$ and $h^* = 0.10$ (movie 4); $h^* = 0.32$ (movie 5). Each animation consists of four videos presented in succession, exploring different flow quantities of interest over the same timescale. The first component highlights the fluid phases (left) and adaptive grid refinement (right) over the full simulation domain, subsequently zooming into the impact region of interest. The next videos show the velocity field components - vertical (left) and radial (right), as well as the magnitudes of the pressure (left) and vorticity (right) fields. Information herein corresponds to cases discussed both in the main text (figure 6) and Supplementary Material (figure S5).